Soft Matter

Design of a microfluidic device for the measurement of the elastic modulus of deformable particles

Journal:	*Soft Matter*
Manuscript ID	SM-ART-11-2018-002272.R1
Article Type:	Paper
Date Submitted by the Author:	17-Dec-2018
Complete List of Authors:	Villone, Massimiliano; University of Naples Federico II, Department of Chemical Engineering Nunes, Janine; Princeton University, Mechanical and Aerospace Engineering Li, Yankai; Tsinghua University, Stone, Howard; Princeton, Mechanical and Aerospace Engineering Maffettone, Pier Luca; University of Naples, Federico II, Department of Chemical Engineering

Journal Name

ARTICLE TYPE

Cite this: DOI: 10.1039/xxxxxxxxxx

Design of a microfluidic device for the measurement of the elastic modulus of deformable particles†

Massimiliano M. Villone,*[a] Janine K. Nunes,[b] Yankai Li,[b] Howard A. Stone,[b] and Pier Luca Maffettone[a]

Received Date
Accepted Date

DOI: 10.1039/xxxxxxxxxx

www.rsc.org/journalname

A microfluidic technique recently proposed in the literature to measure the interfacial tension between a liquid droplet and an immiscible suspending liquid [Hudson *et al., Applied Physics Letters*, 2005, **87**, 081905], [Cabral and Hudson *Lab on a Chip*, 2006, **6**, 427] is suitably adapted to the characterization of the elastic modulus of soft particles in a continuous-flow process. A microfluidic device consisting of a cylindrical pipe with a reduction in cross-section is designed, and the deformation and velocity of incompressible elastic particles suspended in a Newtonian liquid are tracked as they move along the centerline through the constriction. Kinematic and shape information is exploited to calculate the particle's elastic modulus by means of the theory of elastic particle deformation in extensional flow. The approach is validated for different orders of magnitude of the elastic capillary number through experiments and numerical simulations.

1 Introduction

Suspensions carrying soft inclusions occur frequently both in nature and scientific/industrial applications: biological cell suspensions,[1] suspensions of microgel beads or starch granules,[2] and filled polymers[3] are common examples. Of course, the flow properties of such multiphase systems are strongly influenced by the mechanical properties of the suspended particles. Hence, being able to measure material properties can be crucial in order to understand and control the behavior of the above mentioned suspensions. In addition, biological particles, like cells, can suffer modifications of their deformability and function depending on their health state,[4,5] thus measuring their mechanical properties can be a powerful tool to discriminate whether they are healthy or diseased.

In the last twenty years, several methods have been proposed in the literature for the measurement of the mechanical properties of elastic particles and biological cells, such as atomic force microscopy-based techniques,[6–10] micropipette aspiration,[11] compression between parallel plates,[12–15] osmotic compression,[16–22] and capillary micromechanics.[23–27] However, all the aforementioned techniques are intrinsically discontinuous, thus quite time-consuming. Some of them are also quite 'invasive' for the investigated particles, so the measured values of the mechanical properties can be influenced by the contact with the probe of the measuring instrument. On the other hand, in the very recent years, microfluidics is proving to be a suitable tool for the measurement of the mechanical properties of biological cells.[28–35] About a decade ago, Hudson and co-workers developed a continuous-flow non-invasive microfluidic technique providing almost real-time measurement of the interfacial tension between a liquid droplet and an immiscible suspending liquid.[36,37] Compared to other approaches, their method offers considerable advantages in terms of device fabrication and operation ease, low costs, and high throughput.

In this paper, we design a microfluidic device, based on an adaptation of such a technique, for the measurement of the elastic modulus of deformable particles, and we validate it through numerical simulations and experiments on homogeneous synthetic particles with sizes and elasticities in the range of interest for biological cells.[5]

2 Device design

In his early theoretical paper studying an initially spherical incompressible elastic particle suspended in a Newtonian fluid undergoing uniaxial extensional flow in the Stokes regime, i.e., with negligible inertia, Roscoe[38] found that the particle deforms until attaining a steady-state prolate spheroidal shape with the major axis oriented along the extensional axis of the flow. The steady-state deviation of the particle shape from the initial spherical shape can be quantified by means of the (Taylor) steady-state deformation parameter

[a] *Dipartimento di Ingegneria Chimica, dei Materiali e della Produzione Industriale, Università di Napoli Federico II, P.le Tecchio 80, 80125 Napoli, Italy. Tel: +39 081 7682391; E-mail: massimiliano.villone@unina.it*

[b] *Department of Mechanical and Aerospace Engineering, Princeton University, Princeton, NJ 08544, U.S.A..*

† Electronic Supplementary Information (ESI) available: [details of any supplementary information available should be included here]. See DOI: 10.1039/b000000x/

$$D_\infty = \frac{L-B}{L+B}, \tag{1}$$

with L and B the major and minor semi-axes of the spheroid, respectively (see Fig. 1a).

By defining $\alpha_1 = L/R_0$ and $\alpha_2 = B/R_0$, with R_0 the particle initial radius, the deformation parameter at the steady-state can be written as

$$D_\infty = \frac{L-B}{L+B} = \frac{\alpha_1-\alpha_2}{\alpha_1+\alpha_2}. \tag{2}$$

Due to volume conservation, in uniaxial extensional flow, $\alpha_2 = \alpha_1^{-1/2}$, thus from Eq. (2) we get

$$\alpha_1 = \left(\frac{1+D_\infty}{1-D_\infty}\right)^{2/3}. \tag{3}$$

For small deformations (i.e., for $D_\infty \ll 1$), Eq. (104) in Roscoe's paper gives

$$\alpha_1 \simeq 1 + \frac{5}{2}\frac{\eta\dot{\varepsilon}}{G}, \tag{4}$$

where η is the ambient liquid viscosity, $\dot{\varepsilon}$ is the extensional flow strain-rate, and G is the shear elastic modulus of the solid. (We point out that the Poisson ratio of the material used here is $\nu = 0.5$ due to the incompressibility assumption.) Hence, we can write

$$\left(\frac{1+D_\infty}{1-D_\infty}\right)^{2/3} \simeq 1 + \frac{5}{2}\frac{\eta\dot{\varepsilon}}{G}. \tag{5}$$

For $D_\infty \ll 1$, a first-order expansion in series of the left-hand side of Eq. (5) yields

$$\left(\frac{1+D_\infty}{1-D_\infty}\right)^{2/3} \simeq 1 + \frac{4}{3}D_\infty. \tag{6}$$

Therefore, by equating the right-hand sides of Eqs. (5) and (6), we obtain that, when the Reynolds number at the scale of particle is small and the deformation away from a spherical shape is small, the quantitative relation between the steady-state deformation and the material and flow parameters of the system is

$$D_\infty \simeq \frac{15}{8}\frac{\eta\dot{\varepsilon}}{G}. \tag{7}$$

Roscoe's theoretical prediction holds for values of the extensional elastic capillary number $\mathrm{Ca_e} = \eta\dot{\varepsilon}/G \lesssim 0.3$,[39] where $\mathrm{Ca_e}$ represents the ratio of the time scale for particle deformation to the time scale for the particle to move its diameter or, equivalently, the ratio of viscous to elastic stresses.

If an elastic bead suspended in a Newtonian liquid is subject to an abrupt extensional flow, it will reach the D_∞-value corresponding to the imposed flow conditions through a shape evolution. By analogy with liquid droplets,[40] the time-dependent 'driving force' for such evolution can be identified as the difference between D_∞ and the current D-value. For small deformation, we can approximate the time-dependent changes as

$$\frac{dD}{dt^*} = D_\infty - D, \tag{8}$$

with $t^* = t/(\eta/G)$ a dimensionless time, in which η/G is the characteristic time for particle deformation.[38] Equations (7) and (8) can be rewritten as

$$\frac{\eta}{G}\frac{dD}{dt} = \frac{15}{8}\frac{\eta\dot{\varepsilon}}{G} - D, \tag{9}$$

which is conveniently re-expressed as

$$\eta\left(\frac{15}{8}\dot{\varepsilon} - \frac{dD}{dt}\right) = GD. \tag{10}$$

Hence, if one monitors the transient response of an elastic bead to an uniaxial extensional flow with extensional rate $\dot{\varepsilon}(t)$ and measures the deformation parameter $D(t)$ and its time derivative dD/dt, a plot of $\eta(15/8\dot{\varepsilon} - dD/dt)$ versus D should show a linear trend with a slope corresponding to the particle's elastic modulus G. Such a flow measurement then provides a means for measuring G in a continuous-flow process. This argument, which is conceptually analogous to that proposed by Hudson et al. for liquid droplets,[36,37] underlies the design of the microfluidic 'modulometer' proposed below.

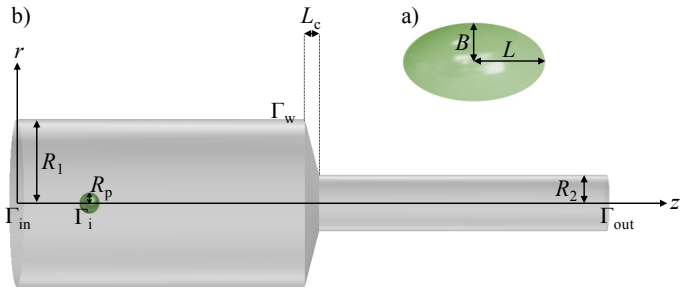

Fig. 1 a) Schematic drawing of an elastic particle deformed into a prolate spheroid. b) Geometry of an initially spherical elastic bead suspended in a Newtonian liquid flowing through a device consisting of two coaxial cylindrical tubes.

In Fig. 1, the geometry of the device is depicted: an initially spherical elastic bead with radius R_p is suspended in a Newtonian liquid flowing through a cylindrical pipe with radius R_1. The entry channel undergoes an abrupt radial contraction to a narrow cylinder of radius R_2. For constructive reasons, the junction between the two coaxial cylindrical tubes may have the shape of a truncated cone with length $L_\mathrm{c} \ll 2R_1$, but, as it will be shown in Sec. 4, L_c can even be zero. A cylindrical coordinate system is set with the origin at the center of the left base of the wide cylinder Γ_in and the axial direction z along the (common) axis of the two cylinders points towards the right base of the narrow cylinder Γ_out. The suspending liquid flows in the positive z-direction, i.e., from Γ_in to Γ_out. The particle is initially placed on the device axis. Placing the particle on the device axis is not a restrictive assumption, since an elastic particle suspended in a Newtonian liquid flowing at low Reynolds number through a circular pipe migrates, due to deformation, transversally to the flow direction from wherever it is initially located to the pipe axis.[41] Hence, provided that the wide tube is long enough, particles will focus on the axis before reaching the contraction.

3 Numerical validation

3.1 Mathematical model and numerical technique

As we want to verify the validity of the approach described in the previous section by means of numerical simulations, we need to provide an adequate mathematical model for the system. Both the suspended particle and the suspending medium are assumed to be incompressible, and we also assume that inertia can be neglected in both phases. Such an assumption is commonly fulfilled in microfluidic flows due to the characteristic flow velocities and length scales involved.[42] Hence, the mass and momentum balance equations for the bead and the fluid read

$$\underline{\nabla}\cdot\underline{u}=0, \tag{11a}$$

$$\underline{\nabla}\cdot\underline{\underline{T}}=\underline{0}, \tag{11b}$$

where $\underline{u}$ is the velocity vector and $\underline{\underline{T}}$ is the stress tensor. The latter, in turn, can be expressed as $\underline{\underline{T}}=-p\underline{\underline{I}}+\underline{\underline{\sigma}}$, with p the pressure and $\underline{\underline{\sigma}}$ the deviatoric contribution to the stress tensor, for which a constitutive equation has to be chosen. For a Newtonian liquid (l), we write

$$\underline{\underline{\sigma}}_{\mathrm{l}}=2\eta\underline{\underline{E}}, \tag{12}$$

with η the liquid viscosity and $\underline{\underline{E}}=(\underline{\nabla u}+\underline{\nabla u}^{\mathrm{T}})/2$ the symmetric part of the velocity gradient tensor $\underline{\nabla u}$. For the elastic particle (p), we choose the neo-Hookean constitutive equation, whose velocity-based formulation is[43]

$$\overset{\triangledown}{\underline{\underline{\sigma}}}_{\mathrm{p}}=2G\underline{\underline{E}}, \tag{13}$$

where the symbol $\overset{\triangledown}{\underline{\underline{\sigma}}}_{\mathrm{p}}\equiv\partial\underline{\underline{\sigma}}_{\mathrm{p}}/\partial t+\underline{u}\cdot\underline{\nabla}\underline{\underline{\sigma}}_{\mathrm{p}}-\underline{\nabla u}^{\mathrm{T}}\cdot\underline{\underline{\sigma}}_{\mathrm{p}}-\underline{\underline{\sigma}}_{\mathrm{p}}\cdot\underline{\nabla u}$ indicates the upper-convected time derivative of $\underline{\underline{\sigma}}_{\mathrm{p}}$ and G the shear elastic modulus of the incompressible solid.

The balance and constitutive equations given above for the liquid medium and the elastic particle are supplied with the following boundary conditions on the inlet Γ_{in}, outlet Γ_{out}, walls Γ_{w}, and the solid-liquid interface Γ_{i}:

$$u_{\mathrm{z}}(r)=2\bar{u}\left[1-\left(\frac{r}{R_1}\right)^2\right]\ \text{on}\ \Gamma_{\mathrm{in}}, \tag{14a}$$

$$\underline{\underline{T}}\cdot\underline{n}_{\mathrm{out}}=-\hat{p}\underline{n}_{\mathrm{out}}\ \text{on}\ \Gamma_{\mathrm{out}}, \tag{14b}$$

$$\underline{u}=\underline{0}\ \text{on}\ \Gamma_{\mathrm{w}}, \tag{14c}$$

$$\underline{u}_{\mathrm{m}}=\underline{u}_{\mathrm{p}}\ \text{on}\ \Gamma_{\mathrm{i}}, \tag{14d}$$

$$\underline{\underline{T}}_{\mathrm{l}}\cdot\underline{n}=\underline{\underline{T}}_{\mathrm{p}}\cdot\underline{n}\ \text{on}\ \Gamma_{\mathrm{i}}. \tag{14e}$$

Equation (14a), with $\bar{u}$ the average velocity of the suspending liquid in the wide entry tube, expresses the parabolic velocity profile arising from the Poiseuille law[44] at the inlet Γ_{in}; Eq. (14b), with $\hat{p}$ the outlet pressure and $\underline{n}_{\mathrm{out}}$ the outwardly directed unit vector normal to Γ_{out}, is the outflow condition at the device outlet; Eq. (14c) gives the no-slip condition on the ambient fluid velocity at the device wall Γ_{w}; finally, Eqs. (14d)-(14e), with the subscript 'l' denoting the liquid, 'p' denoting the particle, and $\underline{n}$ the unit vector normal to the solid-liquid interface and directed towards the liquid, express the velocity and stress continuity across the interface Γ_{i}, respectively.

Since both the particle and the suspending medium are inertialess, no initial condition on the velocity is required, whereas an initial condition is needed on the tensor σ_{p} in the elastic phase. We assume that the particle is initially stress-free, which means

$$\underline{\underline{\sigma}}_{\mathrm{p}}|_{t=0}=\underline{\underline{0}} \tag{15}$$

The above equations are solved using the arbitrary Lagrangian-Eulerian finite-element method using well-known stabilization techniques, namely, SUPG and log-conformation. A detailed description of our numerical approach for suspensions with deformable inclusions is given in Villone *et al.*.[45]

Given the axial symmetry of the system, the actual computational domain is two-dimensional. Both the fluid and the solid particle domains are discretized by a mesh of quadratic triangles. Mesh elements align on the particle-liquid interface (conforming geometry). During the simulations, the elements of the mesh progressively deform because of particle deformation and displacement along the flow direction. In particular, the elements 'upstream' of the particle are stretched, whereas the elements 'downstream' of the particle are compressed by its advancement in the z-direction. Any time the quality of the surface elements in the domain becomes unacceptable in terms of a threshold, a remeshing is performed, and the solution is projected from the old mesh to the new one, as detailed in Hu *et al.*.[46]

Convergence tests have been performed in space and time, i.e., mesh resolution and time-step have been chosen so as to ensure invariance of the numerical solution of the equations presented in this section upon further refinements. Finally, given the model proposed above, we have verified that the distance between the wide tube entrance at $z=0$ and the initial axial position of the particle's geometrical center $z_{\mathrm{p},0}$ is such that the presence of the particle does not perturb the suspending liquid velocity profile for at least a length equal to $2R_1$ after Γ_{in}. In other words, our geometry is suitable to simulate devices whose wide tube's entrance is arbitrarily far upstream of the particle. Moreover, we have checked that the distance between the initial axial position of the particle $z_{\mathrm{p},0}$ and the tube contraction is such that the particle can attain its steady state deformed shape in the wide tube before 'feeling' the effect of the contraction.

3.2 Numerical results

In order to numerically validate the effectiveness of the device proposed above, we choose the wide tube 1500 μm long and 350 μm in radius, the narrow tube 600 μm long and 117 μm in radius, and the junction 60 μm long. Hence, the contraction ratio of the device R_2/R_1 is equal to 1/3. It can be verified that, until L_{c} is within 10% of $2R_1$, the contraction can be considered 'abrupt', thus Eq. (10) holds. Concerning the particle, we consider a bead with a radius of 35 μm and an elastic modulus G = 1 kPa. Finally, the suspending fluid has a viscosity of 0.6 Pa·s, and enters

the device with an average velocity $\bar{u} = 220\,\mu$m/s. Given such information, the shear elastic capillary number in the wide tube is $\mathrm{Ca} = \eta\bar{u}/(2R_1G) \sim 1.9\times10^{-4}$, whereas the confinement ratio of the particle is $\beta = R_p/R_1 = 0.1$. Under those conditions, the steady-state deformed shape of the bead before the contraction does not depart perceptibly from the initial spherical shape.[41]

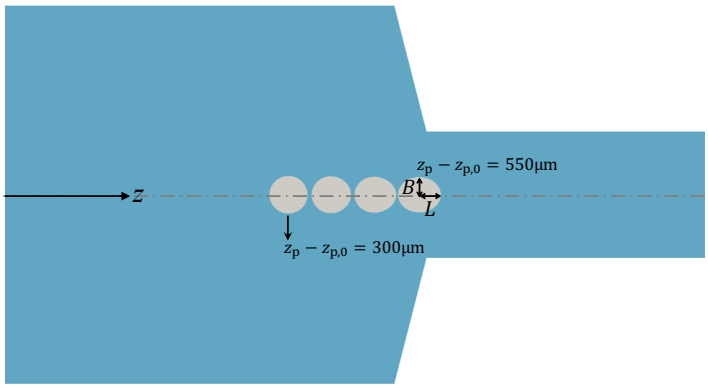

Fig. 2 Sequence of shapes attained by an elastic particle while traveling along the device axis and travelling through the constriction.

We release the undeformed elastic bead at $z_{p,0} = 1000\,\mu$m, then we monitor in 'real-time' how it translates and deforms. In Fig. 2, we report a sequence of four front-views of the shape attained by the particle while it travels along the device axis and goes through the constriction. The first snapshot is taken when the particle is located at $z_p - z_{p,0} = 300\,\mu$m: at that axial position, the deformed shape is hardly distinguishable from the undeformed spherical shape, thus the lengths of the semi-axes L and B are very close to each other. As the bead is displaced along the tube axis, it feels the increasingly intense extensional flow induced by the pipe's cross-sectional reduction, which induces a progressively 'more prolate' spheroidal shape, with the major semi-axis L oriented along the device axis. The last snapshot shown in Fig. 2 is taken at $z_p - z_{p,0} = 550\,\mu$m.

In Fig. 3a, the deformation parameter D is plotted as a function of the axial displacement of the particle with respect to the initial position $z_p - z_{p,0}$. It is evident that, until the particle is far enough from the tube contraction ($z_p - z_{p,0} \lesssim 200\,\mu$m), its deformation is negligible, then, as it experiences the extensional flow induced by the channel cross-sectional reduction, D increases. In the inset in Fig. 3b, the time needed by the particle to reach an axial position is reported versus its axial position: t first increases linearly with $z_p - z_{p,0}$, then, as the particle is affected by the extensional flow, it accelerates (t increases less than linearly with z). From the data displayed in Fig. 3a and in the box in Fig. 3b, the axial profile of the deformation parameter time derivative dD/dt can be obtained (Fig. 3b). In the box in Fig. 3c, the particle's axial velocity $u_{z,p}$ is plotted versus $z_p - z_{p,0}$: 'far' from the contraction, $u_{z,p}$ is constant, then, as the bead feels the extensional field, $u_{z,p}$ increases. The particle's axial velocity is used to obtain the axial profile of the extensional rate $\dot{\varepsilon} \simeq du_{z,p}/dz$ to which the particle is subjected, shown in the main Fig. 3c. Of course, so long as the particle does not feel the extensional field generated by the pipe contraction, $\dot{\varepsilon}$ is null, then, as the bead approaches the contraction, an increase in $\dot{\varepsilon}$ is detected. Notice that we have equated the local extensional rate of the fluid $\dot{\varepsilon}$ with the derivative of the particle's axial velocity in the axial direction $du_{z,p}/dz$. Strictly speaking, this would be correct only if the particle was a tracer, while a slip velocity exists for a particle of finite dimensions, with the particle lagging the fluid. However, since the Reynolds number tends to zero and the particle is on the tube axis, such slip velocity can be neglected.[36,37]

Taking data at the same $z_p - z_{p,0}$ from Fig. 3, a graph of the quantity $\eta(15/8\dot{\varepsilon} - dD/dt)$ as a function of the deformation parameter D can be established. If the theory enunciated in Sec. 2 holds, the points displayed on such a diagram, known as the 'Taylor' plot,[36,37] must fall along a straight line with a slope equal to the particle's elastic modulus G. Indeed, the 'central' data set appearing in Fig. 3.2a can be suitably fitted through a linear function with null intercept and slope equal to 1009.5 Pa (coefficient of determination $R^2 = 0.9998$), represented by the red dashed line. The approach proposed in Sec. 2, then, yields a value of the bead elastic modulus less than 1% different from the 'true' value of 1 kPa (namely, the actual input of the simulation). As a further proof, in Fig. 3.2a, two other series of $\eta(15/8\dot{\varepsilon} - dD/dt)$-versus-$D$ data are displayed: the white diamonds are the outputs of a numerical simulation with a bead having a modulus of 0.1 kPa and the gray triangles come from a simulation where the particle has $G = 10$ kPa (the device geometry and all the operating parameters being the same). These data sets appearing in Fig. 3.2 can be fitted through linear functions with null intercept and slopes equal to 100.71 Pa (coefficient of determination $R^2 = 0.997$, see the green dashed line) and 9998 Pa ($R^2 = 0.998$, cyan dashed line), respectively. Hence, also for particles with an elastic modulus of one order of magnitude lower or higher than the one considered above, our method returns a 'measured' value less than 1% different from the 'true' one. In Fig. 3.2b, the sets of numerical results appearing in Fig. 3.2a are plotted each one scaled by the corresponding estimated value of the elastic modulus $\hat{G}$. As expected, the three series of data all collapse on the bisector of the first quadrant of the Cartesian plane.

4 Experimental validation

4.1 Materials and methods

We produced hydrogel microparticles using a droplet microfluidic method (Fig. 5). Using standard photolithography and soft lithography method,[47] polydimethylsiloxane (PDMS, Sylgard 184, Dow Corning) devices were fabricated containing two focusing junctions. The inner aqueous phase was a photocrosslinkable solution composed of 54 vol% poly(ethylene glycol) diacrylate (PEG-DA, Mn 575 g/mol), 20 vol% 2-dimethylaminoethyl acrylate (DMAEA), 18 vol% deionized water, 8 vol% 2-hydroxy-2-methylpropiophenone (PI) and 5 mg/ml fluorescein o-acrylate. Both oil phases were composed of light mineral oil with 0.5 wt% Span 80 surfactant.

The flow rates of the inner aqueous phase Q_1, the middle oil phase Q_2 and the outer oil phase Q_3 were all controlled independently by syringe pumps (Harvard Apparatus). The inner phase formed droplets in the oil phase at the first focusing junction, which had a concentric geometry to facilitate droplet generation.

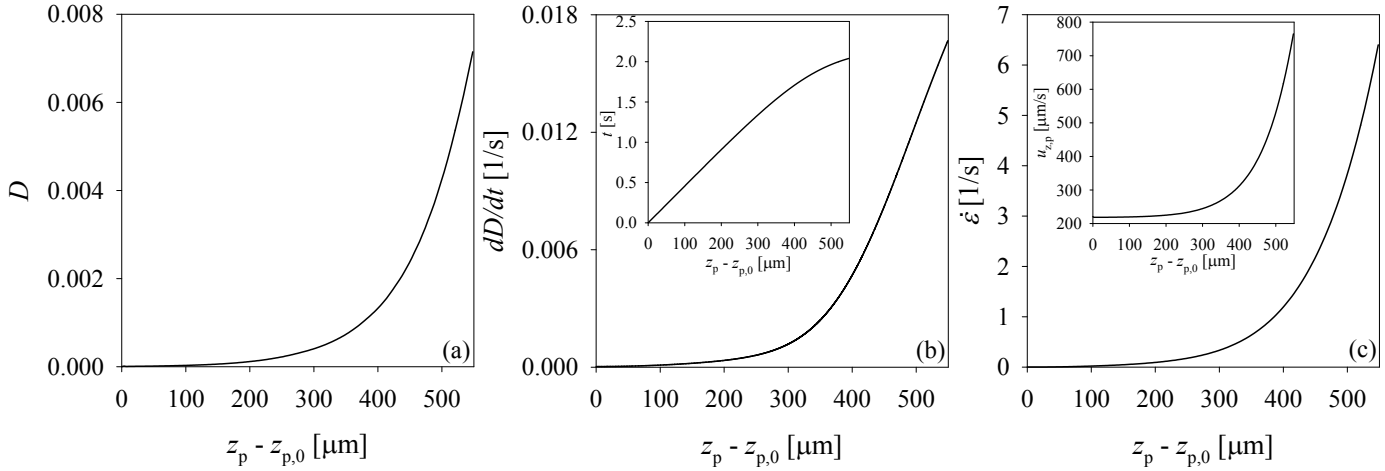

Fig. 3 (a) Axial trend of the deformation parameter D of the elastic particle for the simulation outlined in Fig. 1b. (b) Axial variation of the deformation parameter time derivative dD/dt; inset: time needed by the particle to reach the axial positions reported on the horizontal axis. (c) Axial trend of the extensional rate $\dot{\varepsilon}$ experienced by the particle; inset: axial trend of the particle axial velocity $u_{z,p}$. The constriction goes from $z_p - z_{p,0} = 500\,\mu$m to $560\,\mu$m.

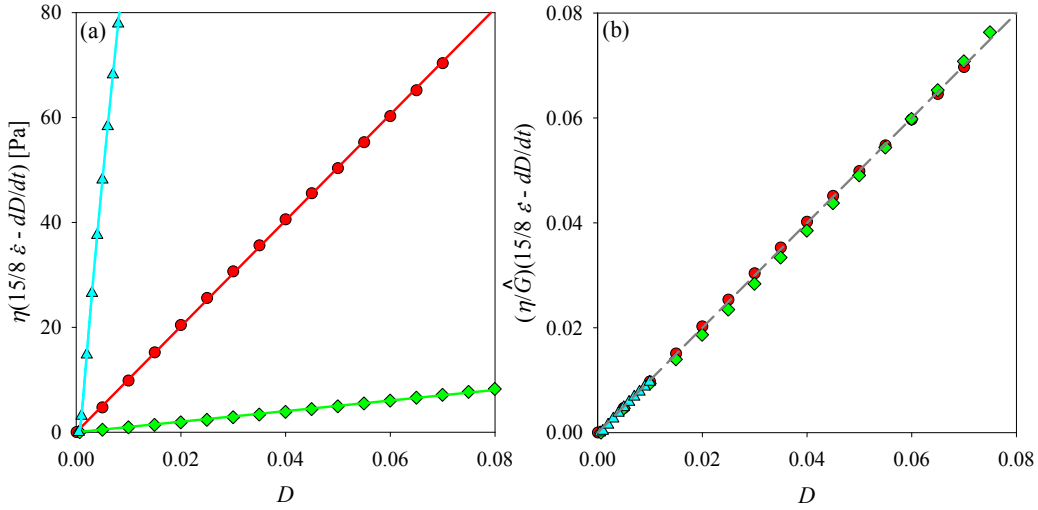

Fig. 4 (a) Green diamonds, red circles, cyan triangles: Taylor plot of $\eta(15/8\dot{\varepsilon} - dD/dt)$ versus D for three different G-values. Green, red, cyan lines: linear fits of the three series of symbols (the slopes are equal to 100.71, 1009.5, 9998 Pa, respectively). (b) Taylor plot of $(\eta/\hat{G})(15/8\dot{\varepsilon} - dD/dt)$ versus D, with $\hat{G}$ the estimated value of the particle shear modulus, for the same data sets as in panel (a).

The size of the droplets was controlled by adjusting Q_1/Q_2; the droplet size was maintained at approximately $100\,\mu$m. After the second junction, the droplets flowed along the main channel and were exposed to a UV light spot approximately 1.4 mm in diameter using a 20X objective on an inverted fluorescence microscope (Leica DMI4000B). The UV intensity ranged between 21 - 29 mW cm^{-2} for all experiments. The exposure time of the droplets, ranging from 150 - 500 ms, was controlled primarily by Q_3, where a higher Q_3 resulted in a shorter exposure time of the droplets, and therefore, a softer particle.

The particles were collected off-chip and washed multiple times in 1 wt% aqueous Tween 80 solution in a series of centrifugation and resuspension steps to remove the oil and unreacted monomer solution. The particles were then washed and resuspended in 0.1 wt% aqueous Tween 80. The particles were stored in 0.1 wt% aqueous Tween 80 for at least 30 hours before testing. Final particle radii, after swelling, ranged from 50 - 125 μm. Immediately before testing, glycerol suspensions were prepared by mixing a 1 - 4 wt% aqueous particle suspension in glycerol (BDH), where the final viscosities of the suspending medium ranged from 0.4 - 0.9 Pa·s. Viscosity was measured with a stress-controlled rheometer (Anton Paar MCR 301). Glycerol solutions were chosen as the suspending media because of the high viscosity required to achieve the range of elastic capillary numbers needed for these measurements, and because the refractive index closely matched that of the PMMA walls of the device. All reagents were obtained from Sigma-Aldrich unless otherwise stated.

For the 'modulometer' device, concentric cylinders were fab-

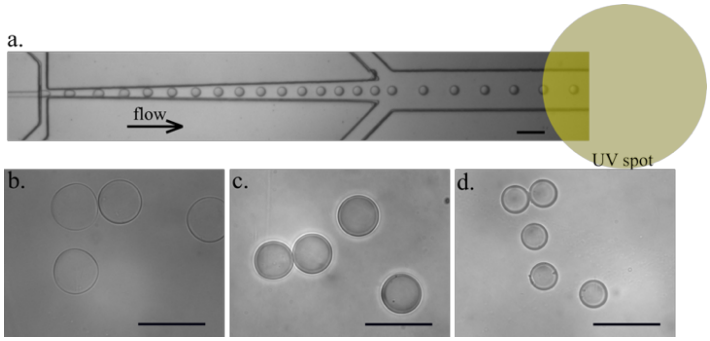

Fig. 5 On-the-fly generation of microparticles in a two-stage microfluidic device. (a) Bright-field microscope image of a section of the microfluidic channel showing monomer droplet generation in oil with the UV exposure region indicated by the yellow circle. Representative images of particles produced at exposure times of (b) 202, (c) 272, and (d) 371 ms. Scale bars represent 250 μm.

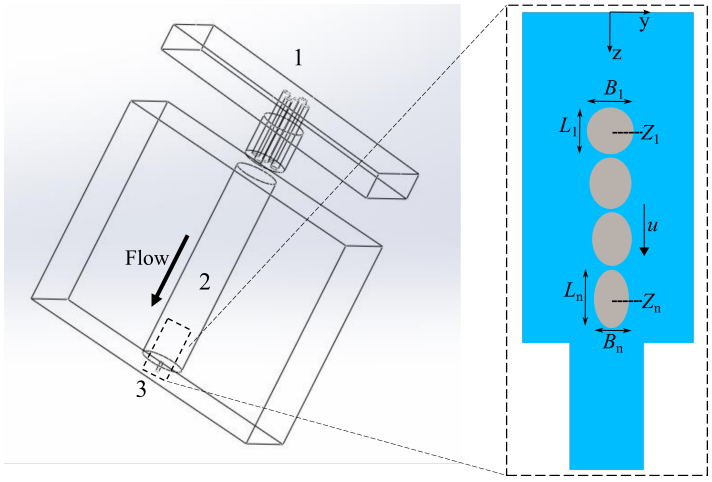

Fig. 6 Sketch of PMMA concentric cylinder device, showing the three main regions, labeled 1-3. On the right is an expanded illustration of the measurement region showing the particle deformations, where L_1, B_1 and Z_1 represent the major and minor semi-axes and the axial position of the undeformed particle. L_n, B_n and Z_n represent the major and minor semi-axes and the axial position of the deformed particle immediately upstream of the constriction, and u is the instantaneous particle velocity.

ricated in polymethylmethacrylate (PMMA) using CNC micro-milling. Each device consisted of three main regions (see Fig. 6). Region 1 is a separate module that can be inserted 3 mm into the main large channel, containing five inlet holes for connecting to the needles and tubing. Region 2 is a large radius cylindrical channel, with $R_1 = 1.5$ mm and length = 15 mm. The channel has an abrupt 90 degree radial contraction, i.e., $L_c = 0$, to a small radius cylindrical channel, $R_2 = 100\,\mu$m and length = 800 μm (region 3 in Fig. 6). Thus, the contraction ratio of the device R_2/R_1 is 1/15. A 27-gauge needle, inner radius 105 μm, was inserted in the central inlet hole and connected via polyethylene tubing to the syringe containing the particle suspension. The surrounding four inlets were connected to the glycerol solutions. We used this configuration to try to ensure that only one particle entered the device at a time and flowed approximately in the center of the channel. We observed that the particles in the suspension flowed individually as they approached the constriction, however many flowed off center such that they only came into focus immediately before entering the smaller channel. These events could not be used to determine G.

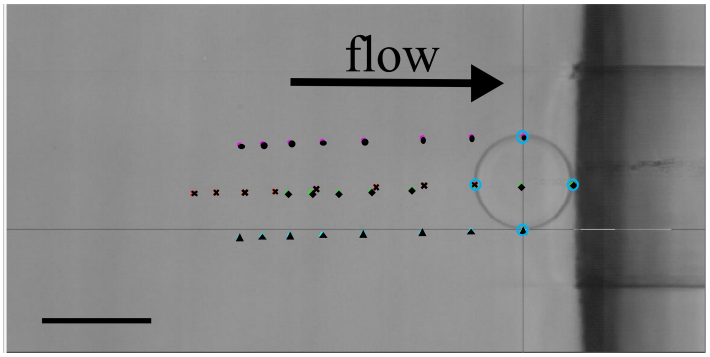

Fig. 7 Tracking the coordinates of the four vertices of the particle at equal time intervals during flow. Flow is from left to right. Scale bar represents 100 μm.

The flow rates of the particle suspension (central inlet) and the glycerol solutions (surrounding inlets) were controlled by syringe pumps (Harvard Apparatus), and the particle deformations immediately upstream of the contraction were recorded with a high-speed camera (Phantom V9.1, Vision Research) mounted on an inverted microscope (Leica DMI4000B) using a 10X objective (1.063 μm/pixel). Images were processed using the i-Speed Suite by Olympus, which tracked the coordinates of four vertices of the particles in each frame (Fig. 7) to determine particle velocities and the deformation parameter D as a function of position. We limited our analysis to small deformations ($D \leq 0.16$ for the softest particles tested). Image sequences from 3 particles per batch were processed. We recall that, assuming that the elastic material is incompressible, the Poisson's ratio $\nu = 0.5$, thus $G = E_Y/3$, where E_Y is Young's modulus.

Separately, the Young's moduli E_Y of the particles in water were measured using a Piuma Nanoindenter (Optics 11). A single force curve was generated per particle for at least 4 particles in the batch, and an average E_Y per particle batch was determined.

4.2 Experimental results

Snapshots of a soft hydrogel particle translating along the center of the large radius channel as it approaches the contraction are displayed in Fig. 8a-g (see also video S1 online, recorded at 5000 fps and played back at 50 fps). Along the centerline and far from the contraction, the axial flow velocity is approximately constant, however, near the contraction, i.e., in the field of view of Fig. 8a-g, the fluid accelerates as it approaches and flows through the contraction (see inset in Fig. 8h), causing an extensional flow field (Fig. 8h). Due to the extensional flow gradient, the particle elongates increasingly with position, with its major axis aligned in the direction of flow. The relationship between the deformation parameter and position, evaluated similar to the numerical simulations in Sec. 3.2, is shown in Fig. 8i. The particle deforms linearly with increasing extensional rate (Fig. 8i inset). The experimentally observed axial trends for $\dot{\epsilon}$, D and dD/dt are consistent with

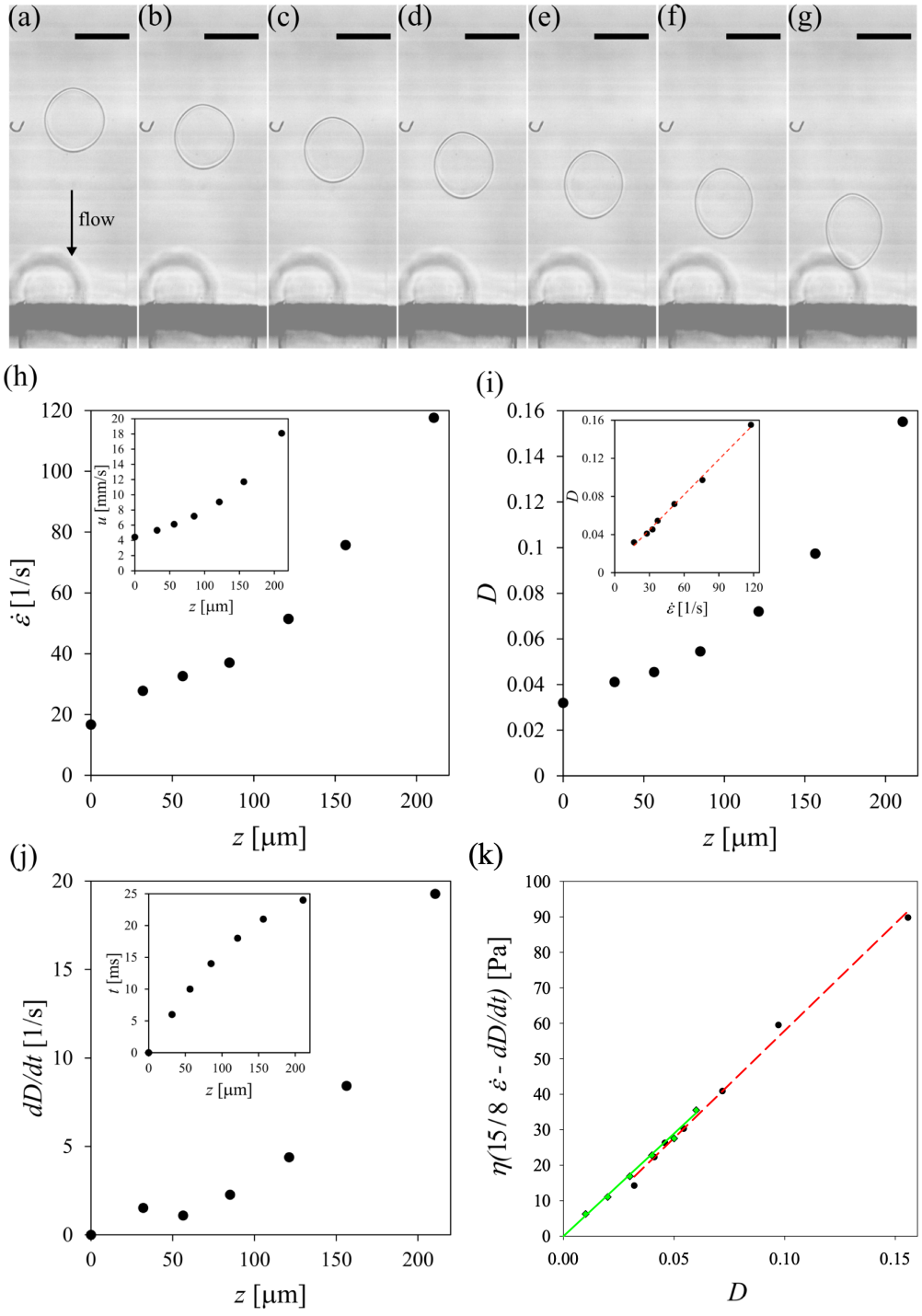

Fig. 8 Example of a typical experimental result. (a-g) Time sequence of a translating hydrogel particle (see also corresponding video S1 online), showing the deformed shape as the particle approaches the contraction, where the extensional rate $\dot{\varepsilon}$ ranges from $16.7 - 118\,\mathrm{s}^{-1}$. Flow is from top to bottom. Scale bars represent $100\,\mu\mathrm{m}$. The blurred circle near the constriction is a mark on the outer surface of the device and does not affect the flow. (h-j) Corresponding axial trends for the hydrogel particle in each frame (a-g) where (h) is $\dot{\varepsilon}$, with an inset showing the axial flow velocity u, (i) is the deformation parameter D, with an inset showing the relationship between D and $\dot{\varepsilon}$, and (j) is dD/dt, with an inset showing the time taken by the particle to reach the corresponding axial position. The constriction starts at z = 340 μm. (k) Taylor plot of the deformation; dashed line is the linear fit with a slope G = 580 Pa. Green diamonds are the outcomes of a numerical simulation with G = 580 Pa and the same parameters as the experiment as inputs. The slope of the green line is 578.8 Pa.

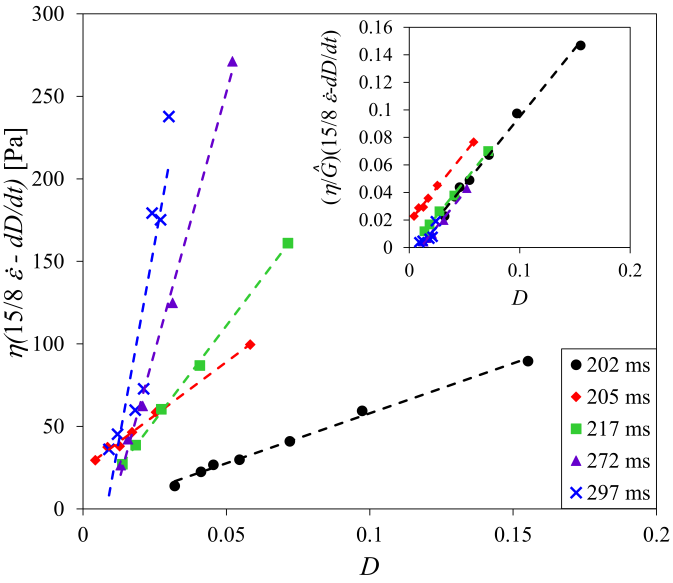

Fig. 9 Deformation plots for particles produced from different exposure times t_{UV}. ○ represents 202 ms, ◇ represents 205 ms, □ represents 217 ms, △ represents 272 ms, and × represents 297 ms. Dashed lines indicate linear fits to the respective data sets. Inset: plot of $(\eta/\hat{G})(15/8\dot{\varepsilon} - dD/dt)$ versus D, with $\hat{G}$ the estimated value of the particle shear modulus, for the same data sets as in the main figure.

Table 1 Comparison of the moduli of particles produced from different UV exposure times t_{UV}, measured using the 'modulometer' and nanoindentation. *Soft particles did not remain spherical during indentation, so E_Y could not be determined by this method.

t_{UV} (ms)	G (kPa) 'modulometer'	$E_Y/3$ (kPa) nanoindentation
202	0.5 ± 0.1	*
205	1.6 ± 0.3	*
217	2.5 ± 0.2	3.2 ± 0.3
272	6.4 ± 0.6	7.0 ± 1.3
297	9 ± 2	23 ± 2

the theory and numerical results described herein (compare to Fig. 3). A Taylor plot of $\eta(15/8\dot{\varepsilon} - dD/dt)$ versus D can be generated for the particle, and the modulus can be determined from the slope (Fig. 8k). The straight line with null intercept of best fit (coefficient of determination $R^2 = 0.9912$) has a slope of 580 Pa. An estimation of the Reynolds number in the wide tube $\mathrm{Re} = 2\rho\bar{u}R_1/\eta$ gives 0.01, thus the model assumption of negligible inertia is fulfilled, while the shear elastic capillary number in the wide tube is $\mathrm{Ca} = \eta\bar{u}/(2R_1G) \sim 7 \times 10^{-4}$, which is comparable with the values considered in the previous section. As a further validation, we report in Fig. 8k also the results of a numerical simulation where the inputted value of the particle modulus is 580 Pa and the other parameters are chosen as to mimic the experiment (see the green diamonds). A fair quantitative agreement is found and the slope of the regression line referring to numerical data is 578.8 Pa.

We produced particles with different crosslink densities by adjusting the UV exposure time t_{UV} of the monomer solution droplets. The Taylor plot in Fig. 9 compares particles prepared with different t_{UV}. The magnitude of the slopes in Fig. 9 increases with increasing t_{UV}, which is consistent with the production of a more highly crosslinked particle when exposed to UV light for longer times. The more crosslinked the particle, the smaller the deformations observed before the particles entered the narrow region of the device. The moduli of the particles were determined from the slopes and compared to the Young's moduli E_Y measured by nanoindentation, as displayed in Table 1. Though we were unable to measure E_Y by nanoindentation for the two softest particle compositions in this study, $t_{UV} = 202$ and 340 ms, due to experimental challenges with the nanoindentation technique, we find that the nanoindentation data is consistent for $t_{UV} = 217$ and 272 ms. The maximum D measured for particles produced at $t_{UV} = 297$ ms was 0.03; for this batch of particles, the difference between the 'modulometer' and nanoindentation results may be the result of an insufficient range of D leading to an imprecise determination of G. For particles produced with $t_{UV} > 297$ ms, the total observable change in L and B before entering the narrow region was ≤ 2 pixels, so G could not be precisely determined. Larger extensional rates than those that were achievable with our setup would be required to deform the more highly crosslinked particles. On the other hand, the results suggest that our method is effective for 'softer' particles, i.e., those produced with $t_{UV} = 217$ and 272 ms, and, as such, warrants further testing and validation.

Our theory assumes that inertia is negligible, particles are small with respect to the radius of the device, and their deformation is small too (in particular, that the extensional elastic capillary number is ≤ 0.3). Even with these assumptions, the 'modulometer' has the potential to probe a large range of particle sizes and moduli, so long as devices can be fabricated to satisfy $R_p/R_1 \ll 1$ and the geometry (with the appropriate flow rates) can produce the necessary extensional rates to sufficiently deform the particle, i.e., to provide a small but measurable D. In addition, the viscosity of the continuous medium can be selected to satisfy $\mathrm{Ca_e} \leq 0.3$, and adjust the characteristic time for particle deformation.

A remark on the major sources of error in determining G by this method: the main measurement errors include the image resolution, and thus our ability to detect the x,y coordinates of the vertices of the ellipse to the nearest pixel $\sim 1\,\mu$m, the video capture frame rate, which determines the smallest time interval, 0.2 ms, which is less than 5% of the time interval between frames used to track the deformation, and experimental error in our viscosity measurement, also ~5%. The second major potential source of errors stems from the theoretical assumptions that may not always match our experimental conditions. For example, the theory neglects wall interactions and approximates the motion of the elastic particle, e.g., the particle may lag the fluid slightly. Also, the particle may not deform to an exactly symmetrical ellipsoidal shape. The theory also assumes incompressibility; based on literature results where the Poisson ratio of bulk PEG-DA hydrogels were measured to be 0.45 - 0.5,[48] we think it is reasonable to assume the particles are incompressible, but there may be a small potential source of error in applying the theory if the Poisson ratio is not exactly 0.5. In addition, in contrast to the theory, we observed that the intercept is not zero in some data plots, as for example, the red diamonds in Fig. 9. This observation can be traced to small initial

non-zero D of the particles at the start of the data collection. In other words, a small error, D_{actual}, allows shifting of the data so that the data would have an intercept of zero. The shift does not affect our ability to use the slope to determine G.

5 Conclusions

In this paper, we explain how to adapt a microfluidic technique recently proposed in the literature[36,37] for the measurement of the interfacial tension between a liquid droplet and an immiscible suspending liquid to the determination of the elastic modulus of soft particles. We design a microfluidic device consisting of a cylindrical pipe with a radial contraction and, by tracking the deformation and velocity of particles suspended in a Newtonian fluid as they go through the constriction, we perform a measurement of their elastic modulus. We validate our approach for different orders of magnitude of the bead elastic modulus through finite-element numerical simulations and experiments. The microfluidic technique proposed in this paper has numerous advantageous aspects, as it is non-invasive, easy to implement, and provides continuous and almost real-time measurements of a particle's mechanical properties. Since experimental testing of the technique is provided for synthetic elastic particles with size- and elasticity-values in the range of interest for biological cells, the application of the modulometer could be extended to biomechanical measurements. On the other hand, it has to be considered that in the mathematical model underlying the device operation it is assumed that the particle is made of an incompressible homogeneous elastic material, which could not always be the case for biological cells.

Conflicts of interest

There are no conflicts to declare.

Acknowledgements

MMV thanks Patrick D. Anderson and Martien A. Hulsen, Eindhoven University of Technology, and Antonio Perazzo, Princeton University, for fruitful discussion. JKN and HAS thank the National Science Foundation (CMMI-1661672). We thank Barry Runner, SEAS Machine Shop, for CNC micromilling and Jiang Li, University of Science and Technology, Beijing, for nanoindentation measurements.

Notes and references

1 M. King and D. Gee, *Multiscale Modeling of Particle Interactions: Applications in Biology and Nanotechnology*, John Wiley & Sons, 2010.

2 M. Desse, D. Fraiseau, J. Mitchell and T. Budtova, *Soft Matter*, 2010, **6**, 363–369.

3 *Smart Polymers: Applications in Biotechnology and Biomedicine*, ed. I. Galaev and B. Mattiasson, CRC Press, Boca Raton, 2007.

4 H. W. Hou, Q. S. Li, G. Y. H. Lee, A. P. Kumar, C. N. Ong and C. T. Lim, *Biomedical Microdevices*, 2009, **11**, 557–564.

5 M. Fraldi, A. Cugno, L. Deseri, K. Dayal and N. M. Pugno, *Journal of the Royal Society Interface*, 2015, **12**, 20150656.

6 H.-J. Butt, B. Cappella and M. Kappl, *Surface Science Reports*, 2005, **59**, 1–152.

7 J. Wiedemair, M. J. Serpe, J. Kim, J.-F. Masson, L. A. Lyon, B. Mizaikoff and C. Kranz, *Langmuir*, 2007, **23**, 130–137.

8 S. M. Hashmi and E. R. Dufresne, *Soft Matter*, 2009, **5**, 3682–3688.

9 V. V. Tsukruk and S. Singamaneni, *Scanning Probe Microscopy of Soft Matter: Fundamentals and Practices*, John Wiley & Sons, 2012.

10 A. Kumachev, E. Tumarkin, G. C. Walker and E. Kumacheva, *Soft Matter*, 2013, **9**, 2959–2965.

11 F. Guilak, J. R. Tedrow and R. Burgkart, *Biochemical and Biophysical Research Communications*, 2000, **269**, 781–786.

12 O. Thoumine, A. Ott, O. Cardoso and J.-J. Meister, *Journal of Biochemical and Biophysical Methods*, 1999, **39**, 47–62.

13 E. A. G. Peeters, C. V. C. Bouten, C. W. J. Oomens and F. P. T. Baaijens, *Medical and Biological Engineering and Computing*, 2003, **41**, 498–503.

14 E. A. G. Peeters, C. W. J. Oomens, C. V. C. Bouten, D. L. Bader and F. P. T. Baaijens, *Journal of biomechanical engineering*, 2005, **127**, 237–243.

15 M. Yuan, X. Ju, R. Xie, W. Wang and L. Chu, *Particuology*, 2015, **19**, 164–172.

16 B. R. Saunders and B. Vincent, *Advances in Colloid and Interface Science*, 1999, **80**, 1–25.

17 A. Fernandez-Nieves, A. Fernandez-Barbero, B. Vincent and F. J. De las Nieves, *The Journal of Chemical Physics*, 2003, **119**, 10383–10388.

18 M. Bradley, J. Ramos and B. Vincent, *Langmuir*, 2005, **21**, 1209–1215.

19 A. F. Routh, A. Fernandez-Nieves, M. Bradley and B. Vincent, *The Journal of Physical Chemistry B*, 2006, **110**, 12721–12727.

20 B. Sierra-Martin, J. A. Frederick, Y. Laporte, G. Markou, J. J. Lietor-Santos and A. Fernandez-Nieves, *Colloid and Polymer Science*, 2011, **289**, 721–728.

21 B. Sierra-Martin, Y. Laporte, A. B. South, L. A. Lyon and A. Fernández-Nieves, *Physical Review E*, 2011, **84**, 011406.

22 J. J. Liétor-Santos, B. Sierra-Martín and A. Fernández-Nieves, *Physical Review E*, 2011, **84**, 060402.

23 H. M. Wyss, T. Franke, E. Mele and D. A. Weitz, *Soft Matter*, 2010, **6**, 4550–4555.

24 M. Guo and H. M. Wyss, *Macromolecular Materials and Engineering*, 2011, **296**, 223–229.

25 T. Kong, L. Wang, H. M. Wyss and H. C. Shum, *Soft Matter*, 2014, **10**, 3271–3276.

26 M. Y. Hwang, S. G. Kim, H. S. Lee and S. J. Muller, *Soft Matter*, 2017, **13**, 5785–5794.

27 Y. Niu, X. Zhang, T. Si, Y. Zhang, L. Qi, G. Zhao, R. X. Xu, X. He and Y. Zhao, *Small*, 2017, **13**, 1702821.

28 J. R. Lange, J. Steinwachs, T. Kolb, L. A. Lautscham, I. Harder, G. Whyte and B. Fabry, *Biophysical Journal*, 2015, **109**, 26–34.

29 A. Mietke, O. Otto, S. Girardo, P. Rosendahl, A. Taubenberger, S. Golfier, E. Ulbricht, S. Aland, J. Guck and E. Fischer-Friedrich, *Biophysical Journal*, 2015, **109**, 2023–2036.

30 O. Otto, P. Rosendahl, A. Mietke, S. Golfier, C. Herold, D. Klaue, S. Girardo, S. Pagliara, A. Ekpenyong, A. Jacobi *et al.*, *Nature Methods*, 2015, **12**, 199.

31 J. R. Lange, C. Metzner, S. Richter, W. Schneider, M. Spermann, T. Kolb, G. Whyte and B. Fabry, *Biophysical Journal*, 2017, **112**, 1472–1480.

32 M. Mokbel, D. Mokbel, A. Mietke, N. Traber, S. Girardo, O. Otto, J. Guck and S. Aland, *ACS Biomaterials Science & Engineering*, 2017, **3**, 2962–2973.

33 K. D. Nyberg, K. H. Hu, S. H. Kleinman, D. B. Khismatullin, M. J. Butte and A. C. Rowat, *Biophysical Journal*, 2017, **113**, 1574–1584.

34 S. Girardo, N. Traeber, K. Wagner, G. Cojoc, C. Herold, R. Goswami, R. Schluessler, S. Abuhattum, A. Taubenberger, F. Reichel *et al.*, *bioRxiv*, 2018, 290569.

35 P. Rosendahl, K. Plak, A. Jacobi, M. Kraeter, N. Toepfner, O. Otto, C. Herold, M. Winzi, M. Herbig, Y. Ge *et al.*, *Nature Methods*, 2018, **15**, 355.

36 S. D. Hudson, J. T. Cabral, W. J. Goodrum Jr, K. L. Beers and E. J. Amis, *Applied Physics Letters*, 2005, **87**, 081905.

37 J. T. Cabral and S. D. Hudson, *Lab on a Chip*, 2006, **6**, 427–436.

38 R. Roscoe, *Journal of Fluid Mechanics*, 1967, **28**, 273–293.

39 T. Gao, H. H. Hu and P. P. Castañeda, *Journal of Fluid Mechanics*, 2013, **715**, 573–596.

40 D. Barthes-Biesel and A. Acrivos, *Journal of Fluid Mechanics*, 1973, **61**, 1–22.

41 M. M. Villone, F. Greco, M. A. Hulsen and P. L. Maffettone, *Journal of Non-Newtonian Fluid Mechanics*, 2016, **234**, 105–113.

42 T. M. Squires and S. R. Quake, *Reviews of Modern Physics*, 2005, **77**, 977.

43 T. Gao and H. H. Hu, *Journal of Computational Physics*, 2009, **228**, 2132–2151.

44 R. B. Bird, W. E. Stewart and E. N. Lightfoot, *Transport Phenomena*, John Wiley & Sons, 1960.

45 M. M. Villone, M. A. Hulsen, P. D. Anderson and P. L. Maffettone, *Computers & Fluids*, 2014, **90**, 88–100.

46 H. H. Hu, N. A. Patankar and M. Y. Zhu, *Journal of Computational Physics*, 2001, **169**, 427–462.

47 D. Qin, Y. Xia and G. M. Whitesides, *Nature Protocols*, 2010, **5**, 491.

48 A. M. Kloxin, C. J. Kloxin, C. N. Bowman and K. S. Anseth, *Advanced Materials*, 2010, **22**, 3484–3494.